NJC

RSC Publishing

PAPER

View Article Online
View Journal | View Issue

Photocatalysis: progress using manganese-doped hematite nanocrystals†

Cite this: *New J. Chem.*, 2013, **37**, 4004

Received (in Montpellier, France) 6th May 2013,
Accepted 10th September 2013

DOI: 10.1039/c3nj00478c

www.rsc.org/njc

Hyun Gil Cha, Hyun Seok Noh, Myung Jong Kang and Young Soo Kang*

Manganese-doped hematite nanocrystals were synthesized by hydrothermal method and study on the activity of photocatalytic properties by different Mn ratio. From the crystal structure and optical study, the oxidation state of the manganese-doped hematite crystals was modulated by doping. The activity of samples (M1–M3) was tested by photodegradation of methyl orange dye in the presence of manganese-doped hematite as photocatalyst.

1. Introduction

Photocatalysts have attracted much attention because of their unique properties and potential applications in all areas of science.[1–6] One of the simple synthetic routes to nanomaterials is probably self-aggregation, in which ordered aggregates are formed in a spontaneous process. However, it is still a big challenge to develop simple and reliable synthetic methods for low-dimensional metal oxide nanostructures with designed chemical components and controlled morphologies which strongly affect the physical/chemical properties. Recently, iron oxides have been investigated extensively because of their wide applications such as ferrofluids, magnetocaloric refrigeration, biotechnology, and *in vivo* bio-medical fields.[7–12] Among iron oxide nanomaterials, hematite (α-Fe_2O_3) is an attractive material for photocatalytic materials because it lies nearly in the optimum range for solar light. This band gap allows absorption of solar energy in the visible region, where the sun emits maximum energy.[13] Besides, hematite is naturally abundant in the earth's crust and is therefore a low cost material. It is also corrosion resistant in acidic and alkaline medium.[14] Removal of organic pollutants (especially, methyl orange (MO) dye) in water has been a significant issue in wastewater treatment because of the non-biodegradable nature of these pollutants. The degradation methods, such as adsorption using activated carbon, coagulation using coagulants, and photocatalytic degradation convert the organic pollutants to small organic compounds. During the past decades, many researchers have put focus on searching for a direct and effective method. In order to improve photocatalytic properties, a facile, safe, and cost-effective method to synthesize metal-doped nanostructured hematite crystals is highly desirable. These dopants have shown to play important roles in improving the optical absorption coefficient, donor density, electrical conductivity, and flat band potential of hematite. Second, nanomaterials with a very large interfacial area between the electrolyte and semiconductor would facilitate the charge collection by reducing the diffusion length for photo-excited holes.[15]

In this work, hematite crystals doped with manganese were prepared by a hydrothermal method. The prepared samples (M1–M3) were characterized for crystal size and *d*-spacing (lattice parameter) with SEM and TEM. The photodegradation yield of methyl orange (MO) dye molecule in the presence of manganese-doped hematite was increased with increasing manganese doping mol% ratio.

2. Experimental details

2.1. Chemicals

Iron(III) chloride hexahydrate ($FeCl_3 \cdot 6H_2O$, 98%), manganese chloride tetrahydrate ($MnCl_2 \cdot 4H_2O$, 98%) used as iron and manganese precursors were purchased from Aldrich Chemical Co. Methyl orange ($(CH_3)_3$:NC_6H_4N:$NC_6H_4SO_3Na$, 99%) used as the photodegraded material and sodium hydroxide (NaOH, 97%) were purchased from Daejung Chemicals & Metals Co., Ltd. All chemical reagents were used as received without further purification. Ultrahigh purity deionized water (>18 MW, Millipore) was used throughout the whole experiment.

2.2. Synthesis of hematite and manganese-doped hematite crystals

The samples were prepared *via* a simple hydrothermal method as follows. An amount of 0.5406 g of $FeCl_3 \cdot 6H_2O$ was dissolved in 10 ml of deionized water, and then 10 ml of 0.4 M NaOH aqueous solution was slowly dropped into the above solution

Korea Center for Artificial Photosynthesis, Department of Chemistry, Sogang University, Seoul 121-742, Korea. E-mail: yskang@sogang.ac.kr; Fax: +82 2 701 0967; Tel: +82 2 705 8882

† Electronic supplementary information (ESI) available: EDX mapping results, line profiles of SAED patterns and SEM images of Mn-doped hematite crystals with different Mn ratio. See DOI: 10.1039/c3nj00478c

with vigorous stirring until the solution cleared. Thereafter different amounts (1–3 mol%) of $MnCl_2{\cdot}4H_2O$ against the Fe source were added into the solution (M1 for 100 : 1, M2 for 100 : 2, M3 for 100 : 3 in mole ratio of Fe to Mn). After adding all of the reactants, the solution was stirred for 1 h at room temperature under vigorous magnetic agitation to ensure homogeneity. The yellow iron oxide solution was then transformed to reddish brown color directly. The resultant system was transferred into a Teflon-lined stainless steel autoclave, sealed and held at 150 °C for 4 h in the oven. Then the resulting particles were centrifuged at 5000 rpm for 10 min and washed with double-distilled water several times. The decanted powder was dried in an oven at 80 °C. The mechanism for crystal nucleation and growth is explained as following;

$$Fe^{3+} + 3OH^- \rightarrow Fe(OH)_3/FeOOH$$

$$FeOOH \xrightarrow{\text{Hydrothermal}} \alpha\text{-}Fe_2O_3$$

As shown above, Fe^{3+} reacted with the OH^- to form the yellow FeOOH suspension. In addition, the yellow FeOOH nanorods freely moved to start to form aggregates with one another longitudinally and laterally by meso-crystal intermediates *via* oriented attachment. This attachment process continues to give rise to cubic shaped structure. These were easily dehydrated during hydrothermal treatment; consequently, Mn-doped hematite crystals could be obtained. During the growth, manganese coordinated with oxygen bonded to Fe atoms.

2.3. Characterization

The morphology of the products was investigated by field emission scanning electron microscopy (FESEM, Hitachi S-4300, Japan) operated at an acceleration voltage of 20 kV. A platinum/palladium alloy (in the ratio 8 to 2) with a thickness of about 15 nm was deposited on top of the samples. The crystal structure of the synthesized materials was characterized by X-Ray diffraction (XRD, Rigaku miniFlex-2 desktop X-Ray diffractometer, CuK_α radiation with $\lambda = 0.154056$ nm, Japan) operating at 30 kV and 15 mA at a scanning rate of 0.02° per step in the 2θ range of $20° \leq 2\theta \leq 80°$. High-resolution transmission electron microscopy (HRTEM, JEM 2100F, Japan) installed with energy dispersive X-ray (EDX) operated at an accelerating voltage of 200 keV was used to analyze the crystal structure and the selected area electron diffraction (SAED) pattern of samples. In these HRTEM experiments, the electron beam was incident along the direction perpendicular to the sample. The nanostructured crystals were transferred onto TEM copper grids by sonicating the substrate in alcohol. EDX spectra were obtained using an Oxford Horiba EX-220 Energy Dispersive X-ray Micro Analyzer (Model: 6853-H). UV-Vis spectra of powder samples were carried out by using a Shimadu UV-310PC (UV-Vis Spectrometer). X-ray photoelectron spectroscopy (XPS) was carried out with K_α (Thermo VG, U.K.) spectrometer using a monochromatic X-ray source (Al K_α = 1486.58 eV). XPS was operated at an accelerating voltage of 12 kV, 3 mA under vacuum for 9.6×10^{-9} mbar. The samples were prepared onto carbon tape and blown by nitrogen gas. The XPS data was calibrated by C1s peak (284.8 eV).

2.4. Photocatalytic degradation of methyl orange (MO) by Mn-doped hematite crystals under 1 sun irradiation

In photocatalyzed reactions, the photocatalytic activity depends on the ability of the photocatalyst to create electron–hole pairs, which generate free radicals (hydroxyl radicals: $^\bullet OH$), which are able to undergo secondary reactions. Generally the photocatalytic reactivity is determined by photodegradation yield of methyl orange (MO) dye with production of the hydroxyl radical ($^\bullet OH$). Hence photodegradation experiments were carried out using a glass reaction cell (4 cm diameter, 8 cm height and 75 ml capacity) covered by a quartz lid. A 1 sun lamp 2.5 W, fixed on the middle of the reaction cell, was used as a light source. During the experiments of photodegradation of MO by 1 sun irradiation in the presence of $\alpha\text{-}Fe_2O_3$ crystals, the initial concentration of MO was fixed at 2.5×10^{-5} mol L^{-1}. 30 mg of photocatalyst was added into the above solution and 0.15 ml of 30% H_2O_2 also added into the solution as a co-catalyst. Before light irradiation, the suspension was stirred for 30 min to let the solids adsorb the organic compound. The first sample for the determination of photodegradation was taken at the end of the dark adsorption period, just before the solution was irradiated, in order to determine the concentration of dye in solution (non-adsorbed). To determine the concentration change of MO during 1 sun irradiation, the same sample amounts of the suspension were taken regularly from the reactor and centrifuged immediately for separation of the suspended solids. The optical absorbance of the clean transparent solution was determined by UV-Vis spectroscopy after centrifugation. The MO concentration was measured from the absorbance at the wavelength of 463 nm by using a calibration curve.

3. Result and discussion

Fig. 1(a and b) shows typical crystallinity of the synthesized as-grown hematite crystals. All the diffraction peaks in this pattern were found to match with the $\alpha\text{-}Fe_2O_3$ phase having rhombohedral geometry (JCPDF card no. 33-0664).[13] The lattice parameters are a = 5.04, c = 13.75, space group $R\bar{3}c$. The sample showed the major characteristic peaks of the grown crystalline metallic iron at 2θ values of 24.2(012), 33.2(104), 35.7(110), 39.4(006), 40.9(113), 43.5(202), 49.5(024), 54.1(116), 57.3(122), 57.6(018), 62.5(214), 64.0(300), 69.6(208), 72.0(119), 75.4(220), and 78.8(223) degrees. These indicate the crystallinity of $\alpha\text{-}Fe_2O_3$ well. From the narrow scan in Fig. 1(b) from 22.5 to 25.5°, the diffraction peaks corresponding to the (012) plane were shifted to a low angle due to extended interplanar space, which corresponds with SAED patterns.

Fig. 1(c) shows the Raman spectrum where the main features are observed at wave-numbers of about 226 (A_{1g}), 245 (E_g), 293 (E_g), 300 (E_g), 412 (E_g), 500 (A_{1g}), and 612 (E_g) cm^{-1} for Fe–O stretching vibration.[17] All bands may be assigned to pure hematite phase. XRD and Raman data of samples indicated that these data were indexed to pure hematite with slight differences in peak intensity.

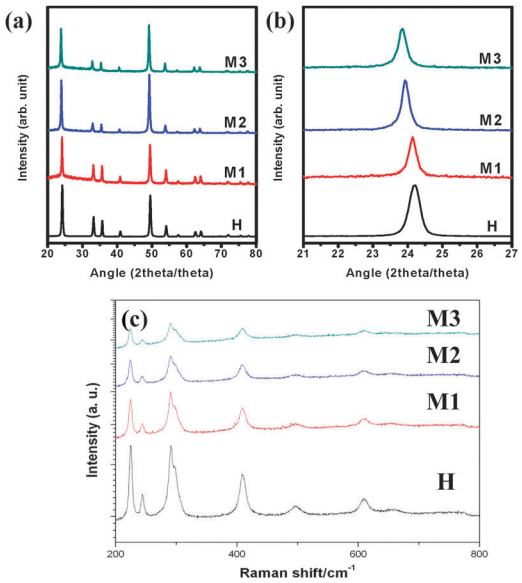

Fig. 1 XRD patterns (a and b, a; wide scan and b; narrow scan) and Raman spectra (c) of Mn-doped hematite from different mole concentrations of Mn source.

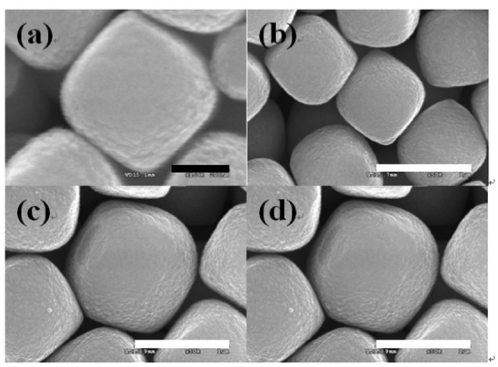

Fig. 2 SEM micrographs show changing average particle size of (a) H (size; 426.8 nm), (b) M1 (size; 734.7 nm), (c) M2 (size; 927.1 nm), and (d) M3 (size; 1216.6 nm). Black scale bar, 200 nm; white scale bar, 1 μm.

The FE-SEM images of as-grown low-dimensional Mn-doped hematite crystals (H, M1, M2, M3) in Fig. 2(a–d) show the low to high magnified images of samples grown by the hydrothermal process. It is clear in the FE-SEM images that the synthesized products have different crystal sizes with different doping amounts of manganese, which were grown in a very high-density and possessed almost uniform cube-like shapes. The increase of the longer axis length of Mn-doped hematite crystals is close to 300 ± 10 nm per added Mn precursor percentage.

The EDX elemental mapping results (Table 1 and Fig. S1, ESI†) of typical Mn-doped hematite crystals revealed that elemental Fe and Mn were both homogeneously distributed inside the crystals without any segregation on the surface or interface. The composition of manganese in samples (M1–M3) is 0.31, 0.37, 0.31 atom%, respectively. This result was also interpreted as the Mn atoms adsorbed on the surface of iron oxide nanorods and then agglomerated to form cubic-shaped Mn-doped hematite crystals.

Table 1 Elemental compositions (weight% and atomic%) obtained by EDX elemental mapping results of selected sample crystal in M1, M2 and M3

	M1		M2		M3	
Element	W[a]	A[a]	W[a]	A[a]	W[a]	A[a]
O	16.83	41.39	14.95	38.03	11.62	31.45
Mn	0.43	0.31	0.50	0.37	0.39	0.31
Fe	82.74	58.30	84.54	61.60	87.99	68.24
Totals	100.00	100.00	100.00	100.00	100.00	100.00

[a] W; weight% and A; atomic%.

In our samples, when the $MnCl_2$ is 1 mole%, the cube shape of Mn-doped hematite crystals with ~740 nm was obtained as shown in the TEM image of the product (Fig. 3(a)). When the concentration of $MnCl_2$ is increased to 2 mole%, uniform Mn-doped hematite crystal cubes appear in the product (Fig. 3(d)). Interestingly, the selected area electron diffraction (SAED) patterns of the samples (M1 and M2) reveal that the product exhibits a single cube, revealing its single crystallinity. The HRTEM images in Fig. 3(b and e) show clear lattice fringes. For nanocubes of

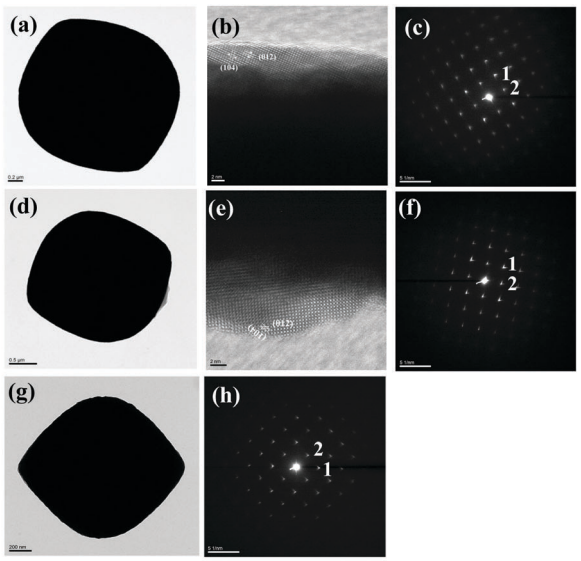

(i)

Sample	# of spot	Crystal plane (hkl)	d-spacing (nm)
M1	1	(012)	0.3734
	2	(110)	0.2547
M2	1	(012)	0.3754
	2	(110)	0.2732
M3	1	(012)	0.3774
	2	(110)	0.2781

Fig. 3 TEM study of prepared samples: (a–c) TEM image, HRTEM image and SAED pattern of M1, respectively. (d–f) TEM, HRTEM image and SAED pattern of M2. (g–h) TEM image and SAED pattern of M3. (i) Summarized interplanar spacing of indicated crystal planes in each sample.

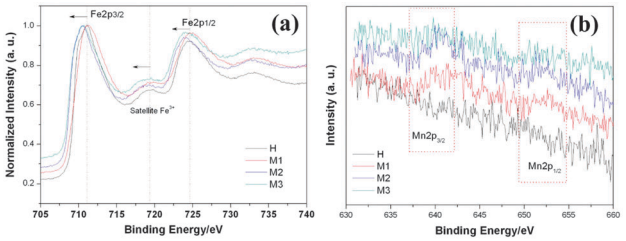

Fig. 4 High resolution Fe2p (a) and Mn2p (b) XPS spectra of H and M1–M3 samples.

M1–M3 samples, both interplanar spacings of (012) and (110) crystal planes of hematite crystal are changed by Mn doping. Based on SAED results, the interplanar space of (012) plane of hematite increased with increasing doping ratio, whereas the (110) plane was decreased Fig. 3(i) and Fig. S2 (ESI†). We suggest that this phenomena was caused by coordination of Mn cations with the surface of iron hydroxide nanorods during the crystal growth *via* oriented attachment growth (Fig. S3, ESI†).[18]

In the high-resolution Fe2p spectra in Fig. 4(a), there were two peaks centered at the binding energies of 724.1 eV for $Fe2p_{1/2}$ and 710.7 eV for $Fe2p_{3/2}$ with a satellite peak at 719.3 eV, which was characteristic of Fe^{3+} in α-Fe_2O_3.[19,20] However, the binding energy of Fe atoms shifts to lower energy with added Mn precursor for preparing Mn-doped hematite crystal. The XPS spectrum of Mn2p in Fig. 4(b) also showed two distinct peaks at binding energies of 640.72 eV for $Mn2p_{3/2}$ and 650.75 eV for $Mn2p_{1/2}$. The binding energy of $Mn2p_{3/2}$ was slightly lower than that of Mn_3O_4 at 640.9 eV (derived from the database of 1999 XPS International, Inc.). These results confirmed that Mn was doped within the lattice of hematite, and mainly bonded with oxygen atoms in the valence state of Mn^{2+} or Mn^{3+}. It caused the chemical and electronic state of Fe on the surface of the crystal to be oxidized to Fe^{3+} instead of Fe^{2+}.

As shown in Fig. 5, the optical absorption measurement was carried out at ambient conditions. The absorption spectra of undoped and Mn-doped hematite crystals are presented in Fig. 5(a). They display an onset of absorption maxima at 520.5 nm in the visible range between 200 to 800 nm wavelengths. The λ_{max} values of pure hematite crystal are quite similar to those reported for α-Fe_2O_3.[16] They show a broad absorption band around 520.5 nm indicating the formation of three dimensional samples having reddish to dark gray colors shown in Fig. 5(c). Band gap energy is calculated on the basis of the maximum absorption band of the samples, and various values are obtained with doping ratio, according to following equation:

$$E_{bg} = 1240/\lambda \text{ (eV)}$$

where E_{bg} is the band-gap energy and λ_{max} is the wavelength of the materials.

From the results, it was observed that the band gap of hematite crystal was reduced with increasing doping ratio of manganese. It was expected that the valence state of hematite was modulated by manganese atoms bonded with oxygen based on the results of UV-vis (Fig. 5(a)) and X-ray photoelectron valence-band spectra (Fig. 5(b)). It visibly shows a color change

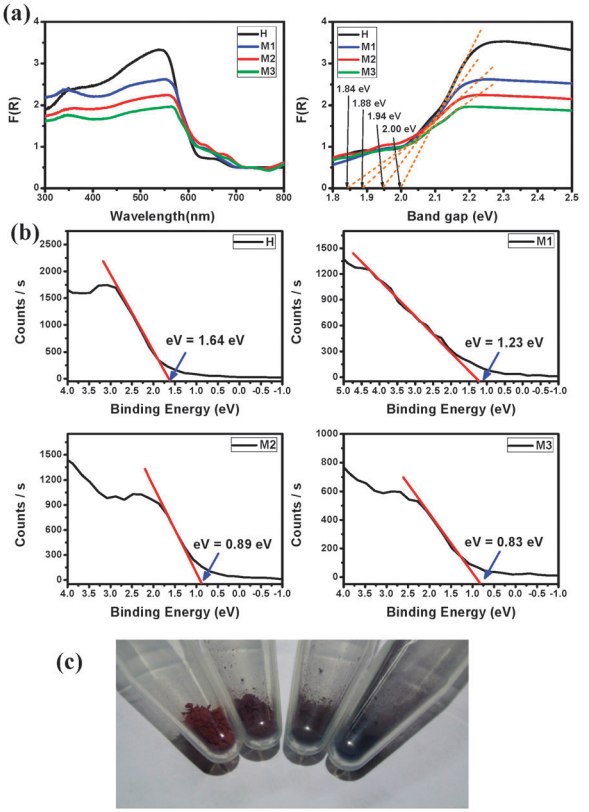

Fig. 5 (a) UV-Vis absorption and bandgap, (b) valence band from XPS survey, and (c) photography of H and M1–M3 samples as per doping ratio.

as shown in the photograph of the samples in Fig. 5(c). Furthermore, the nearly identical widths of their valence bands of about 2.5 eV indicate similar mobility of charge carriers.[21] The existence of oxygen vacancies or impurities can substantially shift the valence band maximum downwards as a result of band blending effects and introduce defect states of Fe^{2+} in the band gap by Mn doping. This is also one of the effects to increase photocatalytic oxidation to produce $^{\bullet}OH^{-}$ radicals.

The molecular structure and absorbance spectra of MO are presented in Fig. 6. The photodegradation of the MO dye occurs predominantly on the manganese-doped hematite crystal surface. The extent of degradation of the MO dye was measured by monitoring its concentration. Fig. 6(a–c) shows the gradual decrease in absorption intensity for the degradation of MO dye as a function of photo-irradiation time. It is observed that the irradiation of an aqueous suspension of MO dye in the presence of manganese-doped hematite crystals leads to a decrease in absorption spectra at 465 nm.

The absorption intensity at 463 nm is significantly decreased with increasing exposure time and gradually decreased until 600 min. It is concluded that the MO dye has is decolorized with sample close to 80%. The decrease in absorption intensity *vs.* irradiation time for the MO in the presence of different doping mol% ratio is shown in Fig. 6(d). It shows a plot for the percent degradation *versus* irradiation time (min) for the oxygen-saturated aqueous suspension of MO in the presence of the photocatalysts of manganese-doped hematite. The degradation of MO clearly

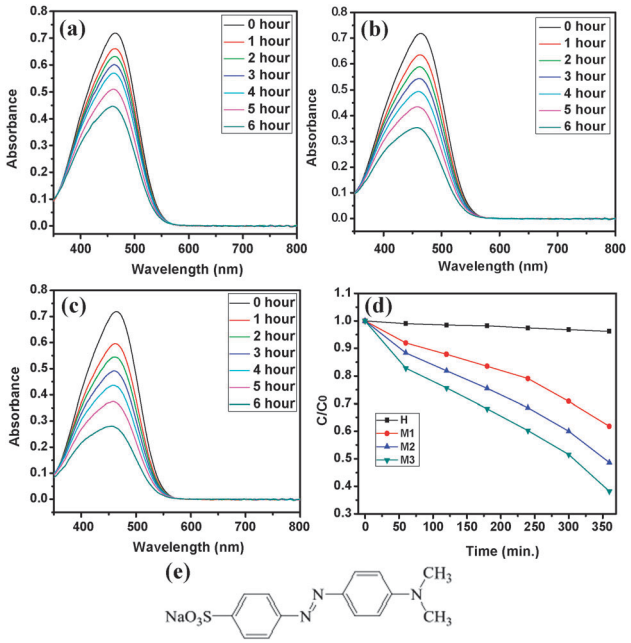

Fig. 6 Photocatalytic degradation of MO using manganese-doped hematite crystals with different Mn mole ratio: (a) M1, (b) M2, (c) M3; (d) degree of MO photodegradation at different time intervals in the presence of Mn-doped hematite crystals, and (e) molecular structure of MO.

demonstrated that prepared Mn-doped hematite crystals possess significant photocatalytic activity and these samples could be beneficial photocatalysts for the removal of colored dyes. The photodegradation of the dye and the photocatalytic reaction follow pseudo first-order kinetics, and it can be described by the relation:

$$\ln(C_o/C) = kt$$

where C and C_o are the actual and initial dye concentrations, and k is the photodegradation rate constant in Table 2. A schematic representation of the MO degradation mechanism is presented in Scheme 1. When the photocatalyst absorbs a photon of energy equal to or greater than its band gap, there will be the formation of an electron–hole pair. If the charge separation is maintained, the electron and hole may migrate to the photocatalyst surface, which can eventually bring about redox reactions of the organic substrates dissolved in water in the presence of oxygen. During the photocatalytic oxidation processes hydroxyl radicals ($^{\bullet}OH$) and superoxide radical anions ($^{\bullet}O^{2-}$) are supposed to be the main oxidizing intermediate species.

These oxidative reactions would result in the mineralization of the dye. Alternatively, direct absorption of light by the MO

Table 2 Summary of size, surface area, and first order kinetic constant of MO degradation

Sample	Size (nm)	S_{BET} ($m^2\ g^{-1}$)	k (h^{-1})
M1	734.7	382.9	0.00123
M2	979.1	368.0	0.00185
M3	1216.6	397.5	0.00241

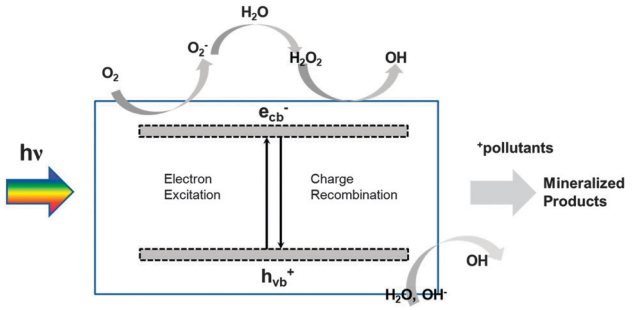

Scheme 1 Schematic representation of MO degradation mechanism.

dye molecules can lead to charge injection from the excited state of MO to the conduction band of the semiconductor, as summarized in the following eqn (i)–(v):

$$\text{Photocatalyst} + h\nu \rightarrow e_{cb-} + h_{vb+} \quad \text{(i)}$$

$$O_2 + e_{cb-} \rightarrow {}^{\bullet}O^{2-} \quad \text{(ii)}$$

$$H_2O + h_{vb+} \rightarrow {}^{\bullet}OH + H^+ \quad \text{(iii)}$$

$$MO_{ads} + h\nu \rightarrow MO_{ads*} \quad \text{(iv)}$$

$$MO_{ads*} + \text{photocatalyst} \rightarrow MO_{ads+} + {}^{\bullet}\text{photocatalyst}\ (e-) \quad \text{(v)}$$

The degradation process was initiated by the photolysis of photocatalyst-oxide/hydroxyl species, and accelerated by solar light, due to the enhanced photolysis of photocatalyst species, which enhances the regeneration of metal precursor with concomitant production of oxide free radicals. Hydroxyl radicals ($^{\bullet}OH$) and superoxide radical anions (O^{2-}) contribute to the oxidation process by attacking the dye molecules and would result in the bleaching of the MO dye. The results above clearly indicate that the photocatalyst prepared by doping with manganese shows increased photocatalytic activity, and thus it can be used as a photocatalyst for the enhanced treatment of wastewater. Based on the results and the mechanism of organic dye removal, the activity of the photocatalyst depends on the parameters of doping ratio and surface area. As shown, sample M3 has higher photocatalytic activity than M1 and M2 even though the amount of Mn ratio was reduced.

4. Conclusions

In summary, the present work provides a hydrothermal method to synthesize undoped and Mn-doped hematite crystals. From this study, we showed the photocatalytic degradation of MO dye by light irradiation (1 sun) and found the almost 100% catalytic photo-degradation functioned with different Mn-doped hematite crystals. The synthesized undoped and Mn-doped hematite crystals have different surface states and electronic structures. The results show different photocatalytic degradation of pollutants. The performance of the proposed manganese-doped hematite crystals might be caused by surface and electronic structures with different mol% doping ratios. This approach also introduces a new route for efficient nanotechnology to control the size of the crystal and lattice parameters as well as light absorption, *i.e.* photocatalyst.

Acknowledgements

This work was supported by the Korea Center for Artificial Photosynthesis (KCAP) located in Sogang University funded by the Ministry of Education, Science, and Technology (MEST) through the National Research Foundation of Korea (No.2012M1A2A2671783).

Notes and references

1 A. Kudo and Y. Miseki, *Chem. Soc. Rev.*, 2009, **38**, 253–278.
2 J. Liu, C. Liang, H. Zhang, Z. Tian and S. Zhang, *J. Phys. Chem. C*, 2012, **116**, 4986–4992.
3 K. Gopalakrishnan, H. M. Joshi, P. Kumar, L. S. Panchakarla and C. N. R. Rao, *Chem. Phys. Lett.*, 2011, **511**, 304–308.
4 J. Barber, *Chem. Soc. Rev.*, 2009, **38**, 185–196.
5 B. O'Regan and M. Gratzel, *Nature*, 1991, **353**, 737–740.
6 M. Gratzel, Recent applications of nanoscale materials: Solar cells, *Nanostructured Materials for Electrochemical Energy Production and Storage*, ed. R. E. Leite, Springer, New York, Ch. 1, 2008.
7 K. Raj, B. Moskowitz and R. Casciari, *J. Magn. Magn. Mater.*, 1995, **149**, 174–179.
8 V. B. Raj, A. T. Nimal, Y. Parmar, M. U. Sharma, K. Sreenivas and V. Gupta Sens, *Sens. Actuators, B*, 2010, **147**, 517–524.
9 M. Saquib, M. A. Tariq, M. Faisal and M. Muneer, *Desalination*, 2008, **219**, 301–309.
10 C. Y. Shen and S. Y. Liou Sens, *Sens. Actuators, B*, 2008, **131**, 673–679.
11 K. V. Sivanand, P. S. Chandrasekaran, Y. Koltypin and A. Gedanken, *Angew. Chem., Int. Ed.*, 1999, **38**, 3521–3528.
12 A. Umar, M. M. Rahman, S. H. Kim and Y. B. Hahn, *Chem. Commun.*, 2008, 166–168.
13 K. Sivula, F. L. Formal and M. Gratzel, *ChemSusChem*, 2011, **4**, 432–449.
14 R. L. Spray, K. J. McDonald and K. S. Choi, *J. Phys. Chem. C*, 2011, **115**, 3497–3506.
15 G. Carraro, D. Barreca, D. Bekermann, T. Montini, A. Gasparotto, V. Gombac, C. Maccato and P. Fornasiero, *J. Nanosci. Nanotechnol.*, 2013, **13**, 4962–4968.
16 H. G. Cha, J. Song, H. S. Kim, W. Shin, K. B. Yoon and Y. S. Kang, *Chem. Commun.*, 2011, **47**, 2441–2443.
17 I. R. Beattie and T. R. Gilson, *J. Chem. Soc. A*, 1983, 980.
18 H. Colfen and M. Antonietti, *Angew. Chem., Int. Ed.*, 2005, **44**, 5576–5591.
19 N. S. McIntyre and D. G. Zetaruk, *Anal. Chem.*, 1977, **49**, 1521–1529.
20 X. L. Hu, J. C. Yu, J. M. Gong, Q. Li and G. S. Li, *Adv. Mater.*, 2007, **19**, 2324–2329.
21 P. Liao and E. A. Carter, *J. Appl. Phys.*, 2012, **112**, 013701.